Roadmap for the Characterization and Validation of Hyperspectral Microscopic Systems

Laura Quintana-Quintana, Gonzalo Rosa Olmeda, Javier Santana-Nunez, Miguel Chavarrías, Samuel Ortega, Jaime Sancho, Himar Fabelo, Eduardo Juárez, *Member, IEEE*, and Gustavo M. Callico, *Senior Member, IEEE*

***Abstract*—Hyperspectral imaging (HSI) is a powerful image technique that allows capturing spatial and spectral information, being able to characterize materials, tissues, and elements in a noninvasive manner. HSI technology is well established at the macroscopic level, but there are still technical challenges to overcome before it can be applied to the microscopic world, such as the lack of standardized characterization methodologies to HS microscopic systems that allow the correct data acquisition as well as ensure the repeatability of the experiments. In this work, we propose a comprehensive roadmap for characterizing and validating such systems, integrating essential parameters highlighted in the current state of the art. Furthermore, we provide a list of the materials needed for their characterization and testing of the methodology on two different HS microscopic systems chosen as representative of common configurations in the field, where an HS camera is integrated into a bright-field microscope. Our proposed roadmap assesses the following parameters: dynamic range (DR), noise quantification, pixel size, spatial frequency response (SFR), spatial scanning accuracy, spatial repeatability, flat-field correction, tone transfer, and spectral sensitivity. We address the challenge of unifying these parameters into a unified and standardized roadmap. All data used to characterize both systems have been captured by the authors. In summary, this comprehensive analysis provides a guideline for the scientific community to develop and characterize HS microscopic systems to ensure reliability, efficiency, and accuracy.**

***Index Terms*—Hyperspectral (HS) imaging (HSI), instrumentation, microscopy, system characterization.**

Received 2 December 2024; revised 25 March 2025; accepted 20 May 2025. Date of publication 4 June 2025; date of current version 24 June 2025. This work was supported in part by the Spanish Government and European Union (FEDER Funds) through the TALENT (HypErsPEctRal Imaging for Artificial Intelligence Applications) under Project PID2020-116417RB-C41 and Project PID2020-116417RB-C42 AEI/10.13039/501100011033; in part by the European Commission through the HORIZON-HLTH-2023-TOOL-05-05, European Project STRATUM (3-D Decision Support Tool for Brain Tumor Surgery), under Grant 101137416; in part the Spanish Ministry of Science and Innovation and European Union (FEDER Funds) through the Open Ai-driven Stack para plataformas hpec mejoradas en Sistemas Integrado (OASIS) Project under Grant PID2023-148285OB-C43 and Grant PID2023-148285OBC44; and in part by the Norwegian Research Council through the IKTPLUSS-IKT og digital innovasjon Project under Grant 332901. The work of Laura Quintana-Quintana was supported in part by the Consejería de Universidades, Ciencia e Innovación y Cultura; in part by the Fondo Social Europeo Plus; and in part by the Agencia Canaria de Investigacion, Innovacion y Sociedad de la Información (ACIISI) of the Consejería de Economía, Conocimiento y Empleo, European Social Fund (FSE) [POC 2014-2020, Eje 3 Tema Prioritario 74 (85%)]. The work of Javier Santana-Nunez was supported by the Investigo Program of Canary Islands Employment Service (Fondos del Plan de Recuperación, Transformación y Resiliencia—Next Generation European Union (EU)), under Grant 32/39/2022-0923131539. The Associate Editor coordinating the review process was Dr. Kamel Haddadi. *(Corresponding author: Laura Quintana-Quintana.)*

Laura Quintana-Quintana and Gustavo M. Callico are with the Research Institute for Applied Microelectronics, University of Las Palmas de Gran Canaria, 35017 Las Palmas de Gran Canaria, Spain (e-mail: lquintana@iuma.ulpgc.es).

Gonzalo Rosa Olmeda, Miguel Chavarrías, Jaime Sancho, and Eduardo Juárez are with the Research Center on Software Technologies and Multimedia Systems, Universidad Politécnica de Madrid, 28040 Madrid, Spain (e-mail: gonzalo.rosa.olmeda@upm.es).

Javier Santana-Nunez is with the Fundación Canaria Instituto de Investigación Sanitaria de Canarias, 35019 Las Palmas de Gran Canaria, Spain, and also with the Research Unit, Hospital Universitario de Gran Canaria Dr. Negrin, 35019 Las Palmas de Gran Canaria, Spain.

Samuel Ortega is with the Norwegian Institute of Food, Fisheries and Aquaculture Research, 9291 Tromsø, Norway, also with the Researcher Department of Mathematics and Statistics, UiT The Arctic University of Norway, 9019 Tromsø, Norway, and also with the Research Institute for Applied Microelectronics, University of Las Palmas de Gran Canaria, 35017 Las Palmas de Gran Canaria, Spain.

Himar Fabelo is with the Research Institute for Applied Microelectronics, University of Las Palmas de Gran Canaria, 35017 Las Palmas de Gran Canaria, Spain.

This article has supplementary downloadable material available at https://doi.org/10.1109/TIM.2025.3575989, provided by the authors.

Digital Object Identifier 10.1109/TIM.2025.3575989

I. Introduction

SPECTRAL analysis techniques allow to gather information noninvasively from the medium by analyzing the response of light interacting with different materials or tissues. This interaction can be produced in terms of transmission, reflection, absorption, and scattering [1]. For this purpose, multispectral or hyperspectral (HS) imaging (HSI) systems are used to record both spatial information and spectral information of a particular scene. Multispectral systems capture a limited number of discrete bands, in the order of tens, while HS systems are able to capture a much larger number of bands, allowing for a more comprehensive spectral analysis [2].

While HSI technology is well established at the macroscopic level [3], [4], [5], the latest integration of HSI with optical microscopy has opened up new opportunities for the analysis of samples at a microscopic scale [6]. This has led to applications such as quality assessment of food products [7], identification of different bacteria and contaminants [8], classification of microplastics [9], [10], or extracting information from microalgae [11]. Fields like cultural forensics or medical imaging [12] have also benefited from microscopic HSI tools to study cultural heritage samples [13], detection of different types of cancers [14], [15], or the identification of different types of blood cells [16].

Currently, the most prominent approach to extract useful information from HS images is the use of machine learning and deep learning techniques [17]. The potential of such techniques relies on training numerous datasets with high amount of HS images, ensuring minimal variation within each class to maintain consistent feature representation and improve classification accuracy [18], [19]. However, the absence of

commercial HS microscopic systems and the extensive use of custom and nonstandardized instrumentation developed by researchers for their standalone application make consistent data acquisition a challenge. Pillay et al. [20] analyze eight different macroscopic commercial HSI systems, and a notorious amount of variability was found among their captures. The data showed spectral, geometric, and colorimetric inaccuracies, along with common residual errors, and substantial differences in noise levels. This variability is likely to be even greater when working with ad hoc systems at the microscopic scale. Thus, despite its potential, the characterization and validation of HS microscopic systems present significant challenges. The lack of standardized procedures for characterizing these systems inhibits their portability across different applications and research groups, resulting in inconsistent results and limited reproducibility [21].

To address the challenge of characterizing HS microscopic systems, several researchers have proposed ad hoc solutions. Ortega et al. [22] developed a custom 3-D printed mechanical system for a precise push-broom HS microscopic system and characterized its robustness by measuring some of its spatial features. Similarly, Stergar et al. [23] introduce a method for spectral characterization by simply measuring the full-width at half-maximum (FWHM) response of their HS microscopic system. Meanwhile, Paterova et al. [24] mixed both spatial and spectral characterization by measuring their system resolution on both dimensions. However, the characterization procedures developed cannot be applied interchangeably to ad hoc HS microscopic systems, underlining the need for standardized methods that can provide consistent results across different setups [21]. These contributions demonstrate a growing interest in characterizing HS microscopic systems, but they also highlight the need for a comprehensive framework that addresses the full range of parameters involved.

To the best of our knowledge, this work is the first to provide a systematic approach to characterizing and validating HS microscopic systems. The contribution of this article includes: 1) a complete list of parameters to be measured; 2) their theoretical background; 3) metrics to evaluate their quality; 4) materials needed for measurement; and 5) descriptions of HS image processing methods required to derive those parameters. While individual methods for specific aspects of characterization are established in the state of the art, their integration into a unified and standardized roadmap, as the one we propose, remains an open challenge. Our structured methodology consolidates these characterization aspects into a single, widely applicable approach, essential to ensure repeatability and comparability across different systems. Our roadmap is proposed within the context of standardization efforts in the field of HSI, as exemplified by the ongoing development of a "Standard for Characterization and Calibration of Ultraviolet through Shortwave Infrared (250–2500 nm) HSI Devices" [25], which does not include guidelines for HS microscopic systems. Additionally, the proposed roadmap is validated through a round-robin test, i.e., an interlaboratory test. Two systems were previously developed by integrating an HS camera into a bright-field microscope, following the common approach for constructing HS microscopic systems [6], [7], [11], [13], [15], [21], [22], [23], [24]. For each system, a different spectral acquisition principle is used as a reference: spatial scanning and linescan wedge HS cameras. In this way, the roadmap is validated and allows the results to be then extrapolated to other types of HS technologies, such as spectral scanning or snapshot-based HS cameras [12].

II. Theoretical Background

This section briefly describes each one of the parameters to be used for the HS microscopic system characterization and validation, providing the necessary background for carrying out the subsequent work.

A. Dynamic Range

The dynamic range (DR) characterizes the variation of the maximum (saturation) and minimum (noise levels) across the spectrum of interest. From the characterization perspective, an exposure time is selected to optimize the DR of the sensor. Furthermore, in HSI capture systems, the DR varies across the spectrum due to differences in the quantum efficiency of the sensor with respect to the wavelengths. The DR for a specific monochromatic image, depicted in (1), is the ratio between the highest intensity captured by the sensor without saturation (N_{sat}) and the lowest intensity captured over the background noise (N_{noise}), i.e., values captured by the sensor when no light interacts with the sensor [26]. In this context, intensity refers to digital values produced by the sensor's analog-to-digital (A/D) converters, which are dimensionless and expressed as digital numbers (DNs). Although these values do not directly represent any physically meaningful magnitude, they are proportional to the detected light intensity based on the sensor's response characteristics

$$\text{DR}\,(\text{dB}) = 20\log\left(\frac{N_{\text{sat}}}{N_{\text{noise}}}\right). \tag{1}$$

The maximum DR that a system can capture depends on the number of bits (n) of the analog-to-digital converter (ADC) of each camera (2). In brief, the higher the DR, the better the ability to quantitatively measure the dimmer intensities within an image; this feature is also known as intrascene performance. Typically, on reflectance-based acquisition systems, a chart compliant with the ISO-21550 standard [27] is used to determine the DR of the system. In the case of transmittance-based systems, an empty sample holder is used

$$\text{DR}_{\text{max}}(\text{dB}) = 20\log\left(2^{n}\right). \tag{2}$$

B. Noise Quantification

All acquisition systems are affected by noise due to the electronics used to convert physical magnitudes into digital values. In the case of digital cameras, whether red, green and blue (RGB) or HS, this noise is due to the movement of electrons in the photoreceptors of the sensors when no photons are interacting with the sensor, which is called dark current (DC) [28]. Quantifying the DC of a system allows the signal-to-noise ratio (SNR) to be calculated. This metric shows how much useful information is captured by an imaging system, where an SNR of 0 dB means that the system cannot discriminate signal from noise. Following the methodology

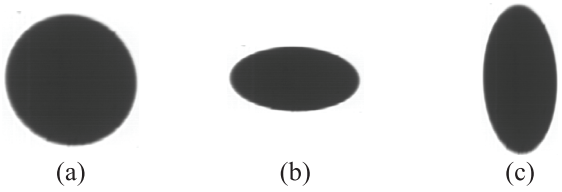

Fig. 1. Dot target captured at different speeds. (a) Optimal speed, (b) too fast, and (c) too slow speed.

proposed by Shaikh et al. [29], the SNR is obtained by capturing an image of a reference target at different exposure times and then capturing an image with the optics completely covered at the same exposure times, to extract the DC. Then, the mean of the HS image is divided by the standard deviation of the DC as follows:

$$\mathrm{SNR\,(dB)} = 20\log\left(\frac{\mathrm{mean\,(HS)}}{\mathrm{std\,(DC)}}\right). \tag{3}$$

As can be observed in both Section II-A and in this Section II-B, only the noise generated by the DC has been considered as the sole noise source. This is because it is the nonimaging error that has the greatest influence on the characterization of the systems, compared to quantum efficiency, gain, or vignetting [30]. In addition, the current state-of-the-art proposes different ways of digitally denoising images, but all of them lack an in-depth analysis of these noise sources [31], [32], [33].

C. Spatial Scanning Accuracy

When integrating a spatial scanning HS camera into a microscopic system, it is crucial for the spatial scanning to be adequate to obtain properly formed HS images. The theoretical platform speed can be established as the ratio between the space captured by one frame and the time required to perform the capture, also known as the frame period. In practice, the frame period may slightly drift from the desired value, and the frames might not be captured synchronized with the platform's stops. Thus, an additional analysis is needed to enhance and validate an accurate system.

The methodology to quantitatively evaluate the spatial scanning accuracy was described by Ortega et al. [22]. In that work, the authors detected camera misalignments and suboptimal movement speeds by assessing the round shape (eccentricity) of a captured circle target. A circle exhibits a flawless round shape when captured at the optimal speed [Fig. 1(a)] but presents an elliptical appearance when the speed is too high [Fig. 1(b)] or too low [Fig. 1(c)]. To quantify how much the ellipse deviates from being a perfect circle, the eccentricity of the circle is calculated at each magnification of the HS microscopic systems. First, 2-D principal component analysis (PCA) is computed over a binary image, generating two eigenvalues ($\phi_{\min}$ and $\phi_{\max}$) that correspond to the directions of the ellipse's longest and shortest axes. From these values, eccentricity can be computed using (4). A perfect circle yields eccentricity values close to zero [22], [34]

$$e = \sqrt{1 - \frac{(\phi_{\min})^2}{(\phi_{\max})^2}}. \tag{4}$$

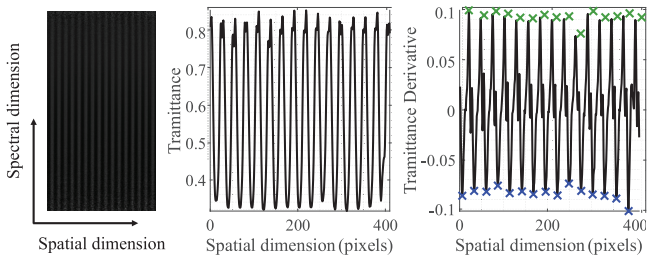

Fig. 2. (a) One-line HS image of the micrometer ruler using System A at 20×. (b) Profile resulting from the spectral average of the one-line HS image. (c) Spatial resolution empirical calculation using the first derivative where green and blue crosses indicate maxima and minima, respectively.

D. Spatial Repeatability

Spatial repeatability can be measured as a metric of a system's ability to produce consistent results under comparable external conditions [35], i.e., the capacity to obtain two equal HS images given the same illumination conditions. Following the methodology developed by Peleg et al. [36], the relative difference (RD) percentage determines the spatial repeatability of an HS system in a particular wavelength. It can be calculated following (5), where "x_i" and "y_i" are the homologous pixel values of the two images to be compared, "i" is the pixel number, and "P" is the total number of pixels in each image [37]. For the RD calculation, images of the micrometer ruler or grid are obtained in a short time span, minimizing the environmental influence over them

$$\mathrm{RD}_{\lambda}\,(\%) = \frac{\sum_{i=1}^{P} |x_i - y_i|}{\left(\frac{1}{P}\sum_{i=1}^{P} x_i + \frac{1}{P}\sum_{i=1}^{P} y_i\right)/2} \cdot 100\%. \tag{5}$$

E. Spatial Resolution

Spatial resolution refers to the ability of an imaging modality to differentiate two adjacent structures as being distinct from one another, a crucial characteristic of imaging systems [38]. The bigger the magnification power, the higher the spatial resolution thus enhancing the ability to distinguish smaller objects. The spatial resolution of the HS microscopic systems can be evaluated theoretically and empirically. The theoretical computation of the spatial resolution (S_R), as shown in (6), considers variables such as pixel size of the sensor (P_S) and magnification (M):

$$S_R = \frac{P_S}{M}. \tag{6}$$

The empirical determination of the pixel size, following the methodology designed by Ortega et al. [22], is performed over a one-line image of a certified micrometer ruler [Fig. 2(a)]. The profile at each wavelength [Fig. 2(b)] is derived to find the local maxima and minima [Fig. 2(c)]. The average spatial distance between lines of the target (0.01 mm in the case of Fig. 2) is divided by the mean distance between local maxima and minima (in pixels), thus empirically determining the size of a single pixel.

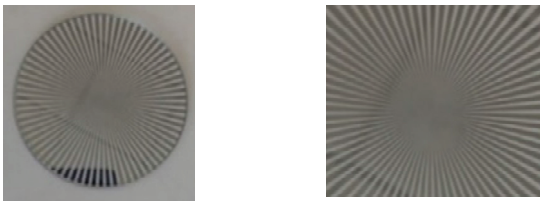

(a) (b)

Fig. 3. (a) Monochromatic image of an HS image of the harmonic modulated Siemens star target and (b) its center showing the aliasing region, where MTF10 is reached [38].

F. Spatial Frequency Response

Spatial resolution is calculated to determine the smallest size of an object that can be detected by the acquisition system at different magnification powers since aliasing may affect resolution. The spatial frequency response (SFR) of a digital imaging system describes its ability to maintain high contrast along certain spatial frequencies. SFR varies with wavelength, influencing spatial resolution across the spectrum, due to diffraction limits (light diffraction is more pronounced at longer wavelengths), sensor sensitivity (sensors may exhibit lower sensitivity at the extremes of the spectrum), and chromatic aberration (optical lenses can cause different wavelengths to focus on slightly different planes). In HSI, an instrument with a high SFR across all wavelengths captured preserves fine spatial details, enhancing spectral accuracy for distinguishing similar materials. This reduces artifacts and supports detailed multiscale analysis [39].

Loebich et al. [38] described a methodology to measure the SFR of a digital camera capturing a Siemens star [Fig. 3(a)]. These are made of sinusoidal oscillations in a polar coordinate system (given by several cycles) so that the spatial frequency decreases for concentric circles of larger radius (5) [38], [39], [40], [41], [42], [43], [44].

The range of spatial frequencies being captured over a monochromatic image is given by the size of the Siemens star, where the Nyquist frequency is the maximum frequency, the sensor is able to capture [42]. For every other spatial frequency, the modulation transfer function (MTF) is measured as a general term of the SFR (6). $I_{\max}$ and $I_{\min}$ refer to, respectively, the maximum and minimum digital values obtained at that specific radius profile [42]. The resolution limit is determined using the r10 criterion [47], which defines the resolution limit as the frequency at which MTF achieves a contrast value of 10%, referred to as MTF10 [38] [Fig. 3(b)]. Emphasis was placed on studying the SFR over wavelengths since diffraction-limited spatial resolution is inversely proportional to wavelength, a relationship first explained by Abbe [46]

$$f(\text{lp/mm}) = \frac{\text{No of cylces}}{2\pi r} \tag{7}$$

$$\text{MTF} = \frac{I_{\max} - I_{\min}}{I_{\max} + I_{\min}}. \tag{8}$$

G. Flat-Field Correction

Flat-field correction is the process employed to correct the variations in the measured radiance values in an HS image caused by the sensor, environmental conditions, and other factors [47]. This step is crucial before continuing with the analysis of the HS data. It involves converting raw DNs, obtained directly from the sensor, into actual radiation intensity [48] or true reflectance values [49], [50], [51]. The process of computing a calibrated HS frame (CI) from a raw HS frame (R) is well established in [22] (9). It is needed a DC capture, explained in Section II-B, and a white reference (WR), the obtention of which depends on the illumination mode. In the transmittance mode, an area of the slide with no sample is usually employed, while in the reflectance mode, a diffuse reflectance standard is used [52]. These standards are frequently constructed with a matte Lambertian reflecting surface, which means that the reflected light has nearly equal intensity in all directions. The total reflection integrated in all directions should be close to 100% [53]

$$\text{CI}(\%) = \frac{\text{R} - \text{DC}}{\text{WR} - \text{DC}} \cdot 100\%. \tag{9}$$

H. Tone Transfer

The calibration process makes an HS image independent of the environment light. However, the so-called tone transfer, the relationship between the optical input and digital signal output, is usually nonlinear [54]. The tone transfer metric examines the significance of the tone transfer between the captured scene and the resulting HS image, allowing to characterize the equilibrium needed among the various spectral bands [55]. Understanding tone transfer is crucial for ensuring accurate data interpretation and improving the reliability of HSI applications across diverse fields, as it directly affects how well the sensor converts light into usable spectral data.

This metric is calculated by capturing the optoelectronic conversion function (OECF) target, which provides a reference on how a sensor converts the illumination it receives into DNs, following ISO-14524 [56]. The mean reflectance of each gray patch at the monochromatic image is calculated and compared to the reference provided by Edmund Optics (Barrington, NJ, USA).

I. Spectral Sensitivity

It is essential to ensure the reliability of HS data by accurately characterizing the spectral response of an HSI system [57]. Spectral sensitivity is the ability of the sensor to detect light as a function of its signal frequency. Typically, the sensitivity of HS camera channels fluctuates through the different wavelengths due to the spectral responsivities of the HS sensor and the nonuniform output from diffractive or filtering elements. Characterizing these irregularities makes it possible to estimate their impact on the captured spectral range [57].

Spectral sensitivity has been analyzed in the state of the art by assessing captured spectra against a ground truth spectrum obtained with a spectrometer [58] or evaluating a captured wavelength calibration standard against a known spectrum [59], [60]. Usually, the latter is preferred for its simplicity. The National Institute of Standards and Technology (NIST) traceable wavelength calibration standards can be employed

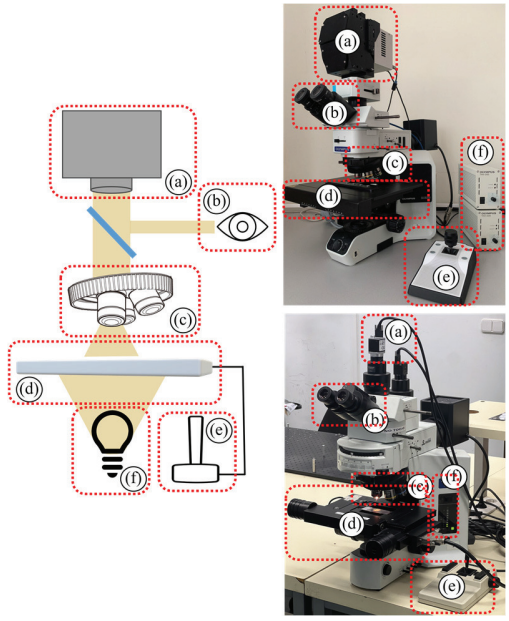

Fig. 4. Diagram of HS microscopic systems (left) and HS microscopic systems employed in this work: System A (top right) and System B (bottom right). (a) HS camera, (b) binoculars, (c) objective lenses, (d) specimen stage, (e) joystick for spatial scanning, and (f) halogen light source.

since they combine rare earth oxides producing very specific absorption peaks, suitable for calibration purposes.

Once the wavelength calibration standard has been captured, the spectral correlation measure (SCM), designed by van der Meero and Bakker [61], quantitatively assesses the spectral quality of the HS image with respect to the reference provided by the manufacturer [62]. SCM is calculated following (10), where n is the number of spectral bands being compared, r is the reference spectral signature given by the manufacturer, and t is the test spectra captured with each HS microscopic system and magnification. The resulting correlation value represents, to some degree, variations in brightness and shape within the spectra

$$\text{SCM} = \frac{n\sum_{i=1}^{n} t_i r_i - \sum_{i=1}^{n} t_i \sum_{i=1}^{n} r_i}{\sqrt{\left(n\sum_{i=1}^{n} t_i^2 - \left(\sum_{i=1}^{n} t_i\right)^2\right)\left(n\sum_{i=1}^{n} r_i^2 - \left(\sum_{i=1}^{n} r_i\right)^2\right)}}. \tag{10}$$

III. Materials and Methods

A. HS Microscopic Systems

To test the proposed roadmap methodology, two HS microscopic systems were set up by coupling HS cameras to two different commercial microscopes via a standard C-Mount. The optical path of the systems starts at the bright-field halogen lamp [Fig. 4(f)] for reflected (top) or transmitted (bottom) illumination. In the transmittance mode, the light travels through the specimen on the stage [Fig. 4(d)] through the selected objective lens [Fig. 4(c)]. In this mode, low magnification enlarges the field of view, increasing the amount of incoming light captured.

In the reflectance mode, the light source is positioned and concentrated above the sample by the objective lens, where it reflects from the sample surface back to the lens. Finally, transmittance/reflectance light is captured by their respective HS camera [Fig. 4(a)]. In this work, System A employs a push-broom HS camera, while System B uses a linescan wedge sensor [63], [64]. Thus, both HS microscopic systems need spatial scanning to generate an HS cube. Custom software was developed to synchronize the movement of the scanning platform with respect to the HS camera frame rate (see Section II-E). Binoculars [Fig. 4(b)] and joystick [Fig. 4(e)] help the operator to visually investigate the sample and move around it to position the field of view in the region of interest to be captured. Table I details the characteristics of the optical and electronic parts of each HS camera and commercial microscope.

TABLE I
HS Microscopic Systems Employed in This Work

		System A	*System B*
Microscope	Model	OLYMPUS BX-53 (Olympus, Tokyo, Japan)	OLYMPUS BX-51 (Olympus, Tokyo, Japan)
	Lenses	LMPLN-IR (5×, 10×), LCPLN-IR (20×, 50×)	UPlanSApo (4×), UPlanApo (10×), PlanApo (40×)
	Halogen lamp	100W TH4 (Olympus, Tokyo, Japan)	100W 7724 (Philips, Amsterdam, Netherlands)
	Wavelength range	400-1800 nm	400-1800 nm
	Light path	Transmittance and reflectance	
	Stage	Scanning stage SCAN 130 × 85 (Märzhäuser, Wetzlar, Germany)	Stage X-Y PRior H101BXDK (Prior Scientific Instruments, Fulbourn, Cambridge, United Kingdom)
HS Camera	Model	Hyperspec® VNIR A-Series (HeadWall Photonics, Fitchburg, MA, USA)	MQ022HG-IM-LS150-NIR (Ximea, Münster, Germany)
	HS technology	Pushbroom	Linescan wedge
	Sensor	CCD (Charge-Coupled Device)	CMOS (Complementary metal-oxide-semiconductor)
	Spectral range	400-1000 nm	470-900 nm
	No. of bands	826	150
	Slit image FWHM	2.5 nm	15.0 nm
	Spatial size of one wavelength	1×1004 pixels	2048×5 pixels
	Pixel size of the sensor	7.4 µm	5.5 µm
	ADC	12 bits	8 bits
	HS cube size	1.6 Mb/line (1×1004×826 bands)	2.5 Gb/cube (2048×1088×150 bands)

FWHM: full width at half maximum. ADC: analog-to-digital converter.

B. Characterization Targets

Here, we display the characterization targets that are needed to measure the parameters under investigation (Fig. 5). For reproducibility, Table II details the manufacturer and specifications of each target employed in the experiments.

C. Proposed Methodology

The methodology, proposed as a roadmap to design and characterize an HS microscopic system, involves assessing the

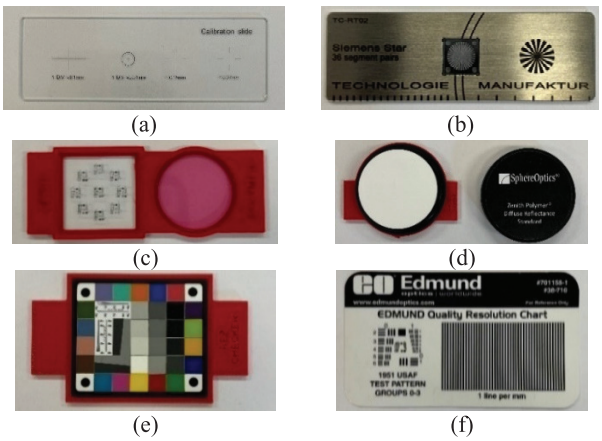

Fig. 5. Characterization targets. (a) Universal calibration slide, (b) Siemens star target, (c) transmittance United States Air Force (USAF) (left) and transmittance wavelength calibration standard (right), (d) reflectance wavelength calibration standard, (e) rez checker matte, and (f) reflectance quality resolution chart.

TABLE II
CHARACTERIZATION TARGETS EMPLOYED IN THIS WORK

Target name	Manufacturer	Specifications
Universal calibration slide (Fig. 2 (a))	Graticules Optics (Tonbridge, UK)	- Coarse grid array: 5 mm/0.5 mm square array + central 2 mm/0.25 mm square, line width 20 µm). - Fine grid array: 5 mm/0.1 mm square array + central 2 mm/0.05 mm square, line width 8 µm) -Dot array: Ø 0.25 mm dot, 0.5 mm spacing, 11×11 grid.
Siemens star target (Fig. 2b))	Edmund Optics (Barrington, NJ, USA)	- 36 sectors. - Spectral range: 200 – 2000 nm - Out diameter: 8 mm. - Tolerance: 100 nm/cm. - OD > [7, 6, 4.5, 3.6] at [400, 550, 750, 1000] nm.
Transmittance wavelength calibration standard (Fig. 2 (c))	Avian Technologies (New London, USA)	- Designation for NIST SRM-2065 standard [65]. -Spectral range: 400-2200 nm. - Focused using the transmittance USAF target.
Reflectance wavelength calibration standard (Fig. 2 (d))	Zenith Polymer® (LabSphere, North Sutton, NH, USA) [52]	- NIST wavelength calibration standard. - Reflectance: 99%, 80%, 50%, and 10%. - Spectral range: 250-2450 nm. - Diameter: 30 mm.
Rez checker (Fig. 2 (e))	Edmund Optics (Barrington, NJ, USA)	- OECF chart: 12 spectrally neutral gray patches.
Reflectance quality resolution chart (Fig. 2 (f))	Edmund Optics (Barrington, NJ, USA)	- Size: 3 ½"× 2". - USAF Pattern: Group 0, Element 1, to Group 3, Element 6. - Ronchi Ruling pattern: 1 line/mm.

OD: optical density, NIST: National Institute of Standards and Technology; USAF: United States Air Force; OECF: features an opto-electronic conversion function.

previously described parameters in a specific order (Fig. 6). First, the exposure time should be configured to maximize the DR and the SNR. Then, spatial resolution and SFR must be acknowledged to ensure that the HS image has the spatial resolution needed for a specific application. If the HS camera needs spatial scanning (e.g., push-broom or line scan), its

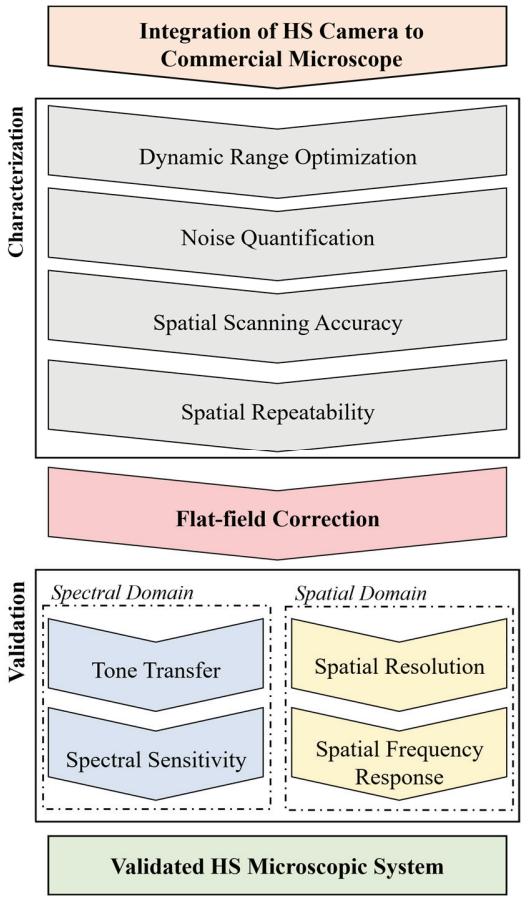

Fig. 6. Proposed roadmap for the characterization and validation of HS microscopic systems.

accuracy must be validated through eccentricity and spatial repeatability parameters. Furthermore, flat-field correction must be performed over the raw HS images; however, the tone transfer between real sample and calibrated images may not be linear. Finally, a spectral sensitivity test would describe the spectral accuracy of the HS microscopic system.

In Section IV, a brief description of each parameter to be used for the HS microscopic system design and characterization will be performed, providing the necessary background for carrying out the subsequent work.

IV. EXPERIMENTAL RESULTS

The results obtained through the previously outlined methodology are presented here. Although both systems operate at various magnifications, in order to improve clarity, only the 10× magnification results are shown in this section for comparison purposes. Data for all other magnifications are provided in the Supplementary Material and are available for comparison with other systems from the state of the art.

A. Characterization of an HS Microscopic System

1) Dynamic Range: The methodology proposed by Shaikh et al. [29] was followed to obtain the DR in both systems. In transmittance, an empty zone of the calibration target [Fig. 2(a)] is captured, increasing the exposure time

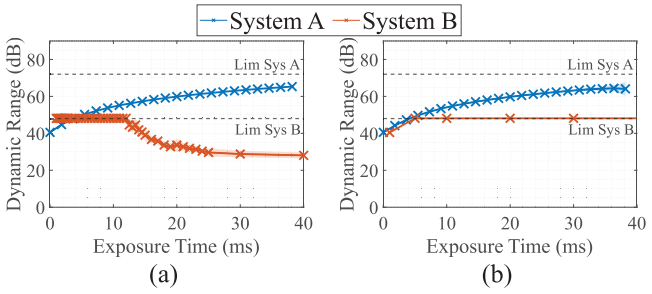

Fig. 7. DR mean and standard deviation for Systems A and B in (a) transmittance and (b) reflectance. The theoretical maximum of DR is 72 and 48 dB for Systems A and B, respectively.

to sweep from the minimum to the maximum exposure time allowed by the camera. The same procedure is followed in reflectance, but in this case, the whitest section of the ISO-21550 standard [Fig. 2(e)] is captured. The brightest pixel and darkest pixel are obtained for each capture to calculate the DR (Table SI of the Supplementary Material). In the transmittance mode, the exposure time values in System A range from 0 to 38 ms in steps of 2 ms and in System B range from 0 to 50 ms, being this range wider and following a nonlinear increment (i.e., $1.1, 1.2, 1.4, 1.6, \ldots, 30, 40$, and 50 ms). In the reflectance mode, the same values as in transmittance mode were employed for System A, and for System B, a range is between 0 and 500 ms following a nonlinear increment (i.e., $1, 5, 10, 20, \ldots, 400, 450$, and 500 ms). These differences in the range of exposure times and the intervals are due to the characteristics of both cameras (see Fig. S1 in Supplementary Material). From the captured values, the DR values are calculated, following (1), for both HS systems and for each magnification (Fig. 7).

Theoretically, the DR of System A can be calculated from the number of bits of the ADC, see Table I, using (2), resulting in 72 dB. From Fig. 7(a), it can be observed that the sensor does not saturate at 10× magnification (it does not at any magnification either, see Fig. S2), due to the low intensity of the emitted light and the relatively short maximum exposure time (40 ms). Thus, its maximum efficiency point would be the highest possible exposure time. Similarly, the maximum DR of System B was calculated to be 48 dB and was tested to quickly saturate at 10× magnification [Fig. 7(b)]. However, since in transmittance, the darkest pixel intensity gradually increases, although the brightest pixel keeps saturating, the DR of System B decreases after reaching its maximum efficiency point, with a loss of 20 dB over the entire remaining range of exposure times.

Exposure times were selected at the point of maximum efficiency: 40 ms for transmittance in System A and 9 ms in System B, with 40 ms for reflectance in both systems. However, as previously noted, System A does not exhibit a distinct maximum efficiency point, so the highest feasible exposure time was chosen for this system. It should be noted that when capturing samples in the transmittance mode, light is sent through the sample, undergoes a few scattering events, and then reaches the objective at the other end of the sample. Thus, the higher the magnification, the thinner

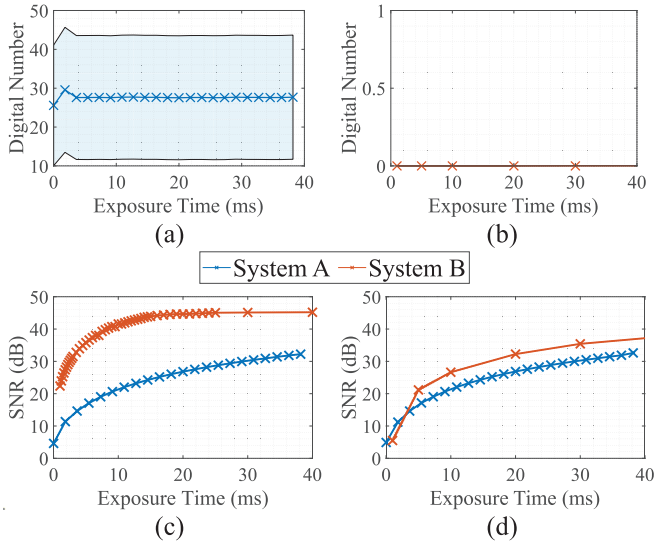

Fig. 8. DC mean and standard deviation values of (a) System A and (b) System B. The maximum DNs are 4095 and 255 for Systems A and B, respectively. SNR for Systems A and B in (c) transmittance and (d) reflectance.

the objective opening, and so less light reaches the sensor [Fig. S2(a) and (c)]. However, in the case of samples captured in the reflectance mode, light is sent from above and only rays with a reflectance angle of 180° are collected by the sensor. In this scenario, lower magnifications, with higher field of view, cause more dispersion and not as much light comes back to the sensor [Fig. S2(b) and (d)]. Therefore, for a given exposure time, smaller magnifications provide higher DR in transmittance than in reflectance.

2) Noise Quantification: To quantify the noise of the HS microscopic systems, the DC was captured over the aforementioned exposure times detailed in Section IV-A1 for each system. The DC signal is captured by completely blocking light from entering the HS camera, avoiding the interaction of the light with the sensor. The HS cameras of Systems A and B work with different numbers of bits (Table I), and thus, the maximum DNs are 4095 and 255, respectively. Considering these values, the results show low and constant DC values for both systems [Fig. 8(a) and (b)]. Comparing the DC standard deviation of System A with respect to System B, the HS sensor of System A has a higher standard deviation, showing a variation of ~30 DNs. This may be due to the systematic offset of 20 DNs that the manufacturer of System A HS sensor applies to avoid the expected noise [66].

Afterward, the SNR is calculated following (3), over a capture of the lighter step of the OECF target [Fig. 2(e)]. In concordance with the previously obtained values, the SNR of System A [Fig. 8(c)] follows a logarithmically increasing behavior from 5 to 35 dB. In terms of System B [Fig. 8(d)], it quickly reaches peak values of 110 and 86 dB for transmittance and reflectance modes, respectively. The behavior is similar among all the magnifications studied (Fig. S3).

3) Spatial Scanning Accuracy: Following the methodology outlined in Section II-E, the alignment of the HS system must be tested to ensure the proper configuration of the scanning parameters. Eccentricity was calculated for each

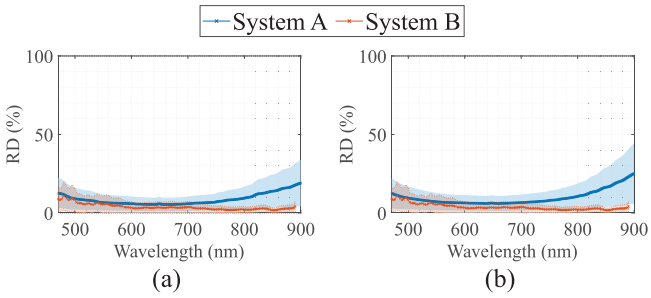

Fig. 9. Spatial repeatability mean and standard deviation for Systems A and B in (a) transmittance and (b) reflectance.

HS microscopic system over all spectral bands, computing the mean and standard deviation values using each available magnification. The obtained values are close to zero (0.037 ± 0.041 for System A and 0.027 ± 0.019 for System B), having System A 27% better eccentricity than System B at $10\times$ magnification. Since both systems produce a mean eccentricity, over all magnifications, of 0.04 and 0.05 for Systems A and B, respectively, it can be established that the platform scanning speed is adequately characterized for the optimal exposure times of each magnification and system configuration (determined in Section IV-A1).

4) Spatial Repeatability: As indicated in Section II-D, the spatial repeatability of the systems has been obtained as the RD of two images of the micrometer ruler. Spatial repeatability results show that transmittance and reflectance have similar mean and standard deviation RD values (Fig. 9). These results are consistent with the SNR values obtained in Section IV-A2 and with the results obtained by Fabelo et al. [37].

When evaluating repeatability across wavelengths, the central spectral bands consistently exhibit better RD performance than those at the extremes due to the quantum efficiency of the sensors. This trend is more evident in System A, which uses a grating to disperse white light, resulting in reduced sensitivity at the spectral limits, which affects the overall performance and reliability of the data in those regions. In contrast, System B, with its filter-based sensor, demonstrates greater consistency across the entire wavelength range. This pattern is persistent when measuring spatial repeatability with other magnification lenses (Fig. S4).

B. Flat-Field Correction

Following the methodology described in Section II-G, an HS image of a transmittance wavelength calibration standard [Fig. 5(c)], composed of 100 lines, was captured in both systems and calibrated using (9). The calibration process is repeated for each raw frame, and finally, to obtain an HS image, a spatial stitch is performed for each frame according to the requirements of the HS technology employed. In addition, only in System B, due to the manufacturer's requirements, it is necessary to apply a spectral correction matrix to sort the bands and obtain the spectral information correctly.

Fig. 10 shows how raw values are different for each system. The radiance range depends on the number of bits of the ADC of the sensor (see Table I for the actual values).

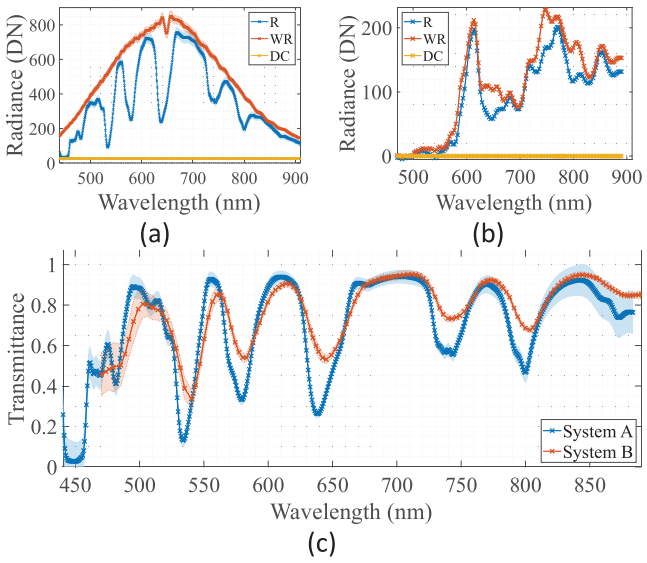

Fig. 10. Mean and standard deviation of the spectral signatures extracted from the raw image (R), WR, and DC of (a) System A and (b) System B. The maximum DNs are 4095 and 255 for Systems A and B, respectively. (c) Calibrated data of both systems. Following the recommendation from a previous study [37], noisy bands have been removed in System A.

However, after calibration, spectral signatures are normalized between 0 and 1, and different HS microscopic system configurations obtain similar spectral signatures.

To assess the accuracy of the flat-field correction, Systems A and B calibrated spectra were compared between them. First, they were interpolated to get the same spectral bands and then correlated using (10), obtaining a value close to one ($\text{SCM} = 0.87 \pm 0.02$). It is worth noticing that System A, using a push-broom camera, requires a straightforward process to conform an HS cube by stitching spatial lines sequentially. On the other hand, System B utilizes linescan wedge technology, involving both spatial scanning and spectral scanning. Thus, achieving the final HS image with System B requires careful manipulation of the lines to account for both spatial information and spectral information. The comparison of both systems spectra with respect to the reference will be shown in Section IV-C4.

C. Validation of an HS Microscopic System

1) Spatial Resolution: To assess the spatial resolution of the HS systems, a micrometer ruler [Fig. 2(a)] was imaged 100 times. At $10\times$ magnification, the empirical spatial resolution (0.739 ± 0.001 μm for System A and 0.558 ± 0.002 μm for System B) closely matches the theoretical values (0.74 μm for System A and 0.55 μm for System B). These results yield a mean RD of 0.13% for System A and 1.45% for System B. When comparing both setups, System B, with a pixel size 24.29% smaller than System A, demonstrates superior spatial resolution, consistent with the sensor pixel sizes of each system (Table I).

2) Spatial Frequency Response: To determine the Nyquist resolution, HS images of the Siemens star target were converted to monochromatic images (by averaging all bands) and divided into eight segments following the methodology

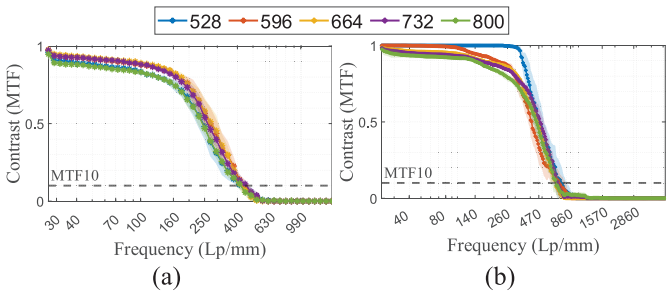

Fig. 11. MTF mean and standard deviation at 10× magnification across different spatial frequencies for (a) System A and (b) System B.

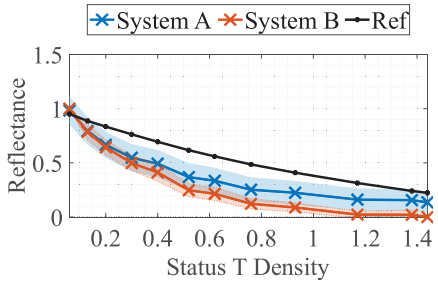

Fig. 12. Mean and standard deviation of the OECF at 10× magnification of Systems A and B. Reference (Ref) is displayed for comparison.

employed in [38]. Then, MTF10 was computed in each segment, following (6), to evaluate the SFR at different regions of the image. At 10× magnification, the high-resolution slide target contains greater Nyquist frequencies (15,485.35 lp/mm for System A and 20,834.83 lp/mm for System B) than those empirically achieved by the microscopes under study (371.02 ± 13.03 lp/mm for System A and 632.29 ± 38.05 lp/mm for System B). It can be determined that System B has a 70% higher limiting frequency than System A, being better at detecting two adjacent objects. These results are consistent with the spatial resolutions of Systems A and B at this magnification.

Furthermore, the SFR was evaluated for each system at different wavelengths (Fig. 11). In this case, each single-band image was also divided into eight segments to check the SFR at different regions of the images. The mean MTF values at each configuration follow the same trend, starting at maximum contrast where all white and dark lines are distinguishable ($I_{max} = 1$, $I_{min} = 0$, and MTF = 1), to the point of no contrast, where black and white lines are mixed into gray ($I_{max} = 0.5$, $I_{min} = 0.5$, and MTF = 0). Consistent results showed that the lower the wavelength, the higher the MTF10 (Fig. S5), following Abbe's approximation [46] of the diffraction limit.

However, no linear relationship was found between the limiting resolutions at different wavelengths in any of the systems. For example, a decrease from 800 to 528 nm, which represents a reduction of 34% in wavelength, produced an increase of the limiting spatial frequency of 9% at System A and 44% at System B. The discussion of the crucial balance between resolution and wavelength was also described by the Rayleigh criterion equation ($R = 0.61\lambda/\text{NA}$) [67], [68]. For a given numerical aperture (NA), lower wavelengths (λ) provide a higher resolution, which is characterized by a lower value of the minimum resolvable distance (R), providing the instrument's capability to discern closely spaced objects. However, some limitations, such as the noise produced by the systems and the uncertainty of the SFR methodology [53], provide nonlinear results, showing the necessity of further investigations in this field.

3) Tone Transfer: Although flat-field correction helps to standardize the HS image with respect to the illumination and sensor employed, several gray tones absorb differently onto the sensor (see Section II-H). The mean and standard deviation reflectance was calculated for each gray step of the OECF target [Fig. 2(e)]. Results show, far from a linear relationship,

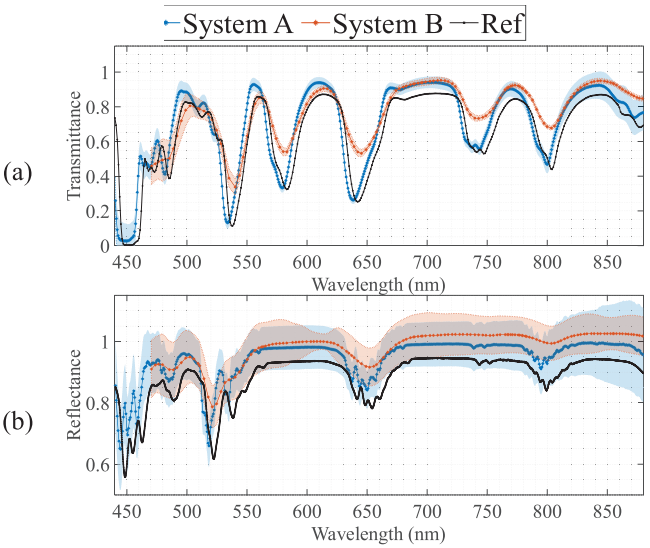

Fig. 13. Mean and standard deviation of Systems A and B signatures from the NIST wavelength calibration standard for (a) transmittance and (b) reflectance.

an exponential decay of the reflectance with respect to the optical density of the sample (Fig. 12). Root-mean-square error (RMSE) was calculated between Systems A and B with respect to the reference, providing close to zero values (0.201 ± 0.063 for System A and 0.275 ± 0.015 for System B). However, while System B deviates more from the reference, reaching a closely zero reflectance value for a status T density of 1.38, System A has greater differences between the obtained mean reflectances (Fig. S6).

4) Spectra Sensitivity: The last parameter being tested is the spectra sensitivity of the HS microscopic systems. Following Section II-I, 100 lines of the transmittance and reflectance NIST wavelength calibration standards [Fig. 2(c) and (d), respectively] were captured at transmittance and reflectance (Fig. 13). To measure the spectra sensitivity of the HS microscopic systems, the obtained spectral signatures were compared, using the SCM metric, to the NIST reference provided by the manufacturer (transmittance: 0.876 ± 0.008 for System A and 0.911 ± 0.024 for System B; reflectance: 0.590 ± 0.074 for System A and 0.771 ± 0.096 for System B).

As presented in Section IV-A1, transmittance captures tend to represent the reference more accurately than reflectance captures and, thus, their smaller standard deviation. At 10×,

System B provides better SCM results than System A, 4% and 21% for transmittance and reflectance, respectively. At other magnifications, System B also presents higher SCM values, ranging from 0.5 to 0.9 (Fig. S7).

V. Discussion

Understanding the performance parameters of a microscopic HS system is essential for ensuring accurate data capture and analysis. To support future developers and users/operators of HS microscopic systems, we offer practical suggestions for implementing the methodology proposed in this article, which should be followed in the given order.

1) Examine the DR of the microscopic HS system to set its optimal exposure time. Transmittance measurements generally offer more DR than reflectance ones.
2) Assess DC and SNR to know when the captures are reliable. Some sensors have a constant DC settled by the manufacturer (e.g., for System A is 20).
3) Evaluate spatial resolution, especially when differentiating small-sized spatial features, such as identifying cells on a histology slide, where achieving high spatial resolution is essential. Use a micrometer ruler, however, there may be a misidentification of spatial frequencies due to aliasing. Thus, assessing SFR is essential, particularly Nyquist resolution, is important. Lower wavelengths yield better SFR, following the essential connection between resolution and wavelength, as outlined by the Rayleigh criterion. To understand the limitations of an HSI system in terms of spatial frequency, measurements should be conducted at longer wavelengths.
4) Determine the appropriate platform velocity for HS cameras requiring spatial scanning, once the optimal exposure time and spatial resolution have already been determined. To check proper alignment, circles should be captured, and their eccentricity checked for each magnification. This step is not necessary for those HS microscopic systems that do not require spatial scanning (i.e., spectral scanning and snapshots HS systems).
5) Identify spatial repeatability using consecutively captured HS cubes to evaluate the robustness of the microscopic HS system. Most probably it experiences a decline at extreme bands, where the SNR is usually lower due to the quantum efficiency of the sensor.
6) Perform flat-field correction once HS cubes can be properly captured. This step serves to standardize HS captures by mitigating the impact of variations in the surrounding light environment. Afterward, the image should be assembled following its HSI technologies (i.e., push-broom or linescan wedge).
7) Analyze tone transfer, as flat-field correction standardizes HS captures but does not address reflectance variation. Typically, the analysis reveals an exponential decay of the reflectance with respect to optical density.
8) Quantify spectral sensitivity, which becomes essential when analyzing spectral properties of the materials under investigation and aiming to identify specific absorption peaks. While HS microscopic systems typically offer strong spatial sensitivities, fluctuations in SNR have the potential to cause specific spectral signatures to deviate more significantly from the established reference standard. Systematically identify and quantify these fluctuations to correct and enhance spectral analysis reliability.

TABLE III
Summary of Best-Performing HS Microscopic System for Each Parameter Studied

Parameter	Metric	*System A*		*System B*	
		T	R	T	R
Dynamic range	Exposure time (ms)	40	40	9	40
	Dynamic range (dB)	65.3 ± 0.1	64 ± 4	48.1± 0.1	48.1 ± 0.1
Noise quantification	SNR (dB)	32.2 ± 0.1	32.6 ± 0.1	103.97 ± 1	93.2 ± 20
Spatial scanning accuracy	Eccentricity	0.04 ± 0.04	N/A	0.03 ± 0.02	N/A
Spatial repeatability	Relative difference (%)	14 ± 8	16 ± 9	4 ± 3	4 ± 2
Spatial resolution	Spatial resolution (μm/pixel)	0.739 ±0.001	N/A	0.558 ± 0.002	N/A
Spatial frequency response	Modulation transfer function (lp/mm)	370 ± 10	N/A	630 ± 40	N/A
Tone transfer	Mean reflectance	N/A	0.20 ± 0.06	N/A	0.28 ± 0.02
Spectral sensitivity	Spectral correlation measure	0.88 ± 0.01	0.59 ± 0.07	0.91 ±0.02	0.77 ± 0.10

*T: Transmittance. R: Reflectance. N/A: Not applicable.

Moreover, Table III provides a summary of the values obtained at 10× for each HS microscopic system, determining which one better satisfies each characterization and validation parameter (Table SI completes these data by showing results at all possible magnifications for each system). This information may serve as a valuable reference for future developers and users/operators of HS microscopic systems, enabling them to compare their results with those presented in this article. It must be noted that spatial scanning, accuracy, spatial resolution, and SFR were not evaluated in the reflectance mode due to the unavailability of specific targets. Similarly, tone transfer in the transmittance mode could not be tested.

System B employs a linescan sensor composed of spectral filters arranged side by side, requiring scanning of the entire sensor over the sample to capture material data. This design excels in spatial parameters, capturing the 2-D scene simultaneously and enhancing spatial resolution and frequency response. Additionally, System B offers a superior DR, making it particularly suitable for applications demanding high spatial precision and DR, such as detailed analysis of microscopic structures. However, the complexity of system assembly can be seen as a drawback.

Conversely, System A uses a push-broom HS camera that diffracts a ray of light from a spatial line to capture all its spectral bands simultaneously, offering a plug-and-play solution. This characteristic simplifies the system setup and operation, making it more accessible for various applications. System A is superior for high spectral resolution tasks, capturing

826 bands compared to the 150 bands of System B. This makes it ideal for applications that require detailed spectral information, such as identifying specific chemical compositions or detecting subtle spectral features.

VI. Conclusion

The lack of a standard methodology to characterize and validate HS microscopic systems limits their transferability between different applications and research teams, leading to variability in results and reduced reproducibility. This lack of standardization also makes the formal validation of HS microscopic systems challenging. However, a methodology based on well-established procedures for characterizing the different optical and spectral properties of imaging systems could solve this issue. The main contribution of this article is to provide a structured roadmap to characterize and validate HS microscopic systems to improve repeatability and enable comparison across various systems. To the best of our knowledge, this is the first time in which a unified methodology has been proposed for this purpose, potentially serving as a foundation for incorporating HS microscopic systems into the "Standard for Characterization and Calibration of Ultraviolet through Shortwave Infrared (250–2500 nm) HSI Devices." Furthermore, the proposed roadmap has been validated through a round-robin test using two different HS microscopic systems to test its generalizability. Future research in the field would employ the proposed roadmap as a technical verification for the development of HS microscopic systems. Reporting the quality metrics of these systems would enhance the publicly available characterization information, which can improve reproducibility and standardize the technical validation of the public microscopic HS image datasets.

References

[1] S. L. Jacques, "Optical properties of biological tissues: A review," *Phys. Med. Biol.*, vol. 58, no. 11, pp. R37–R61, Jun. 2013, doi: 10.1088/0031-9155/58/11/r37.

[2] H. Grahn and P. Geladi, *Techniques and Applications of Hyperspectral Image Analysis*. Hoboken, NJ, USA: Wiley, 2007.

[3] B. Wang et al., "The applications of hyperspectral imaging technology for agricultural products quality analysis: A review," *Food Rev. Int.*, vol. 39, no. 2, pp. 1043–1062, Feb. 2023, doi: 10.1080/87559129.2021.1929297.

[4] S.-E. Qian, "Hyperspectral satellites, evolution, and development history," *IEEE J. Sel. Topics Appl. Earth Observ. Remote Sens.*, vol. 14, pp. 7032–7056, 2021, doi: 10.1109/JSTARS.2021.3090256.

[5] J. Yoon, "Hyperspectral imaging for clinical applications," *BioChip J.*, vol. 16, no. 1, pp. 1–12, Mar. 2022, doi: 10.1007/s13206-021-00041-0.

[6] K. S. Banu, M. Lerma, S. U. Ahmed, and J. L. Gardea-Torresdey, "Hyperspectral microscopy-applications of hyperspectral imaging techniques in different fields of science: A review of recent advances," *Appl. Spectrosc. Rev.*, vol. 59, no. 7, pp. 935–958, Aug. 2024, doi: 10.1080/05704928.2023.2270035.

[7] B. Park, T. Shin, J.-S. Cho, J.-H. Lim, and K.-J. Park, "Improving blueberry firmness classification with spectral and textural features of microstructures using hyperspectral microscope imaging and deep learning," *Postharvest Biol. Technol.*, vol. 195, Jan. 2023, Art. no. 112154, doi: 10.1016/j.postharvbio.2022.112154.

[8] A. Soni, Y. Dixit, M. M. Reis, and G. Brightwell, "Hyperspectral imaging and machine learning in food microbiology: Developments and challenges in detection of bacterial, fungal, and viral contaminants," *Comprehensive Rev. Food Sci. Food Saf.*, vol. 21, no. 4, pp. 3717–3745, Jul. 2022, doi: 10.1111/1541-4337.12983.

[9] T. Kitahashi et al., "Development of robust models for rapid classification of microplastic polymer types based on near infrared hyperspectral images," *Anal. Methods*, vol. 13, no. 19, pp. 2215–2222, May 2021, doi: 10.1039/d1ay00110h.

[10] A. Faltynkova, G. Johnsen, and M. Wagner, "Hyperspectral imaging as an emerging tool to analyze microplastics: A systematic review and recommendations for future development," *Microplastics Nanoplastics*, vol. 1, no. 1, pp. 1–19, Dec. 2021, doi: 10.1186/s43591-021-00014-y.

[11] Z. Xu, Y. Jiang, J. Ji, E. Forsberg, Y. Li, and S. He, "Classification, identification, and growth stage estimation of microalgae based on transmission hyperspectral microscopic imaging and machine learning," *Opt. Exp.*, vol. 28, no. 21, p. 30686, Oct. 2020, doi: 10.1364/oe.406036.

[12] S. Ortega, M. Halicek, H. Fabelo, G. M. Callico, and B. Fei, "Hyperspectral and multispectral imaging in digital and computational pathology: A systematic review [invited]," *Biomed. Opt. Exp.*, vol. 11, no. 6, p. 3195, Jun. 2020, doi: 10.1364/boe.386338.

[13] B. Males, L. H. Oakley, O. Cossairt, and M. Walton, "Maximizing the microscope: Instrument design and data processing strategies for hyperspectral imaging of cross-sectional cultural heritage samples," *Proc. SPIE*, vol. 11058, pp. 24–31, Jul. 2019.

[14] E. Aloupogianni et al., "Hyperspectral imaging for tumor segmentation on pigmented skin lesions," *J. Biomed. Opt.*, vol. 27, no. 10, Oct. 2022, Art. no. 106007, doi: 10.1117/1.jbo.27.10.106007.

[15] L. Ma, J. V. Little, A. Y. Chen, L. Myers, B. D. Sumer, and B. Fei, "Automatic detection of head and neck squamous cell carcinoma on histologic slides using hyperspectral microscopic imaging," *J. Biomed. Opt.*, vol. 27, no. 4, Apr. 2022, Art. no. 046501, doi: 10.1117/1.jbo.27.4.046501.

[16] Q. Huang, W. Li, B. Zhang, Q. Li, R. Tao, and N. H. Lovell, "Blood cell classification based on hyperspectral imaging with modulated Gabor and CNN," *IEEE J. Biomed. Health Informat.*, vol. 24, no. 1, pp. 160–170, Jan. 2020, doi: 10.1109/JBHI.2019.2905623.

[17] S. Prasad and J. Chanussot, *Hyperspectral Image Analysis*. Cham, Switzerland: Springer, 2020.

[18] A. Atla, R. Tada, V. Sheng, and N. Singireddy, "Sensitivity of different machine learning algorithms to noise," *J. Comput. Sci. Colleges*, vol. 26, pp. 96–103, Jun. 2011.

[19] A. Saseendran, L. Setia, V. Chhabria, D. Chakraborty, and A. B. Roy, "Impact of noise in dataset on machine learning algorithms," *Mach. Learn. Res.*, vol. 2019, pp. 1–8, Jul. 2019.

[20] R. Pillay, M. Picollo, J. Y. Hardeberg, and S. George, "Evaluation of the data quality from a round-robin test of hyperspectral imaging systems," *Sensors*, vol. 20, no. 14, p. 3812, Jul. 2020, doi: 10.3390/s20143812.

[21] H. Pu, L. Lin, and D.-W. Sun, "Principles of hyperspectral microscope imaging techniques and their applications in food quality and safety detection: A review," *Comprehensive Rev. Food Sci. Food Saf.*, vol. 18, no. 4, pp. 853–866, Jul. 2019, doi: 10.1111/1541-4337.12432.

[22] S. Ortega et al., "Hyperspectral push-broom microscope development and characterization," *IEEE Access*, vol. 7, pp. 122473–122491, 2019, doi: 10.1109/ACCESS.2019.2937729.

[23] J. Stergar, R. Hren, and M. Milanič, "Design and validation of a custom-made hyperspectral microscope imaging system for biomedical applications," *Sensors*, vol. 23, no. 5, p. 2374, Feb. 2023, doi: 10.3390/s23052374.

[24] A. V. Paterova, S. M. Maniam, H. Yang, G. Grenci, and L. A. Krivitsky, "Hyperspectral infrared microscopy with visible light," *Sci. Adv.*, vol. 6, p. 44, Oct. 2020, doi: 10.1126/sciadv.abd0460.

[25] *GRSS/SC—Standards Committee Standard for Characterization and Calibration of Ultraviolet Through Shortwave Infrared (250 Nm To 2500 Nm) Hyperspectral Imaging Devices*, Standard P4001, 2018.

[26] M. A. Robertson, S. Borman, and R. L. Stevenson, "Dynamic range improvement through multiple exposures," in *Proc. Int. Conf. Image Process.*, Aug. 1999, pp. 159–163.

[27] Photography Electronic Scanners for Photographic Images Dynamic Range Measurements, ISO Standard 21550:2004, 2004.

[28] C. Pan et al., "Analysis of OMPS in-flight CCD dark current degradation," in *Proc. IEEE Int. Geosci. Remote Sens. Symp. (IGARSS)*, Jul. 2016, pp. 1966–1969.

[29] M. S. Shaikh, K. Jaferzadeh, and B. Thörnberg, "Extending effective dynamic range of hyperspectral line cameras for short wave infrared imaging," *Sensors*, vol. 22, no. 5, p. 1817, Feb. 2022, doi: 10.3390/s22051817.

[30] D. H. Foster and K. Amano, "Hyperspectral imaging in color vision research: Tutorial," *J. Opt. Soc. Amer. A, Opt. Image Sci.*, vol. 36, no. 4, p. 606, Apr. 2019, doi: 10.1364/josaa.36.000606.

[31] T. Zhang, Y. Fu, and J. Zhang, "Guided hyperspectral image denoising with realistic data," *Int. J. Comput. Vis.*, vol. 130, no. 11, pp. 2885–2901, Nov. 2022, doi: 10.1007/s11263-022-01660-2.

[32] B. Rasti, P. Scheunders, P. Ghamisi, G. Licciardi, and J. Chanussot, "Noise reduction in hyperspectral imagery: Overview and application," *Remote Sens.*, vol. 10, no. 3, p. 482, Mar. 2018, doi: 10.3390/rs10030482.

[33] X. Guo, X. Huang, L. Zhang, and L. Zhang, "Hyperspectral image noise reduction based on rank-1 tensor decomposition," *ISPRS J. Photogramm. Remote Sens.*, vol. 83, pp. 50–63, Sep. 2013, doi: 10.1016/j.isprsjprs.2013.06.001.

[34] D. Cohen, *Precalculus: With Unit Circle Trigonometry*, 4th ed., Boston, MA, USA: Cengage Learning, 2005.

[35] A. S. Lister, "7 validation of HPLC methods in pharmaceutical analysis," in *Handbook of Pharmaceutical Analysis By HPLC*, vol. 6. Amsterdam, The Netherlands: Elsevier, 2005, pp. 191–217.

[36] K. Peleg, G. L. Anderson, and C. Yang, "Repeatability of hyperspectral imaging systems—Quantification and improvement," *Int. J. Remote Sens.*, vol. 26, no. 1, pp. 115–139, Jan. 2005, doi: 10.1080/01431160412331291288.

[37] H. Fabelo et al., "In-vivo hyperspectral human brain image database for brain cancer detection," *IEEE Access*, vol. 7, pp. 39098–39116, 2019, doi: 10.1109/ACCESS.2019.2904788.

[38] C. Loebich, D. Wueller, B. Klingen, and A. Jaeger, "Digital camera resolution measurement using sinusoidal Siemens stars," *Proc. SPIE*, vol. 6502, pp. 214–224, Feb. 2007.

[39] U. Artmann, "Quantify aliasing a new approach to make resolution measurement more robust," *Electron. Imag.*, vol. 31, no. 10, pp. 320–326, Jan. 2019, doi: 10.2352/issn.2470-1173.2019.10.iqsp-320.

[40] S. J. Yoon, P. Bajcsy, M. Litorja, and J. J. Filliben, "Evaluation of lateral resolution of light field cameras," *Opt. Eng.*, vol. 57, no. 9, p. 1, Sep. 2018, doi: 10.1117/1.oe.57.9.093101.

[41] G. C. Birch and J. C. Griffin, "Sinusoidal Siemens star spatial frequency response measurement errors due to misidentified target centers," *Opt. Eng.*, vol. 54, no. 7, Jul. 2015, Art. no. 074104, doi: 10.1117/1.oe.54.7.074104.

[42] U. Artmann, "Linearization and normalization in spatial frequency response measurement," *Electron. Imag.*, vol. 28, no. 13, pp. 1–6, Feb. 2016, doi: 10.2352/issn.2470-1173.2016.13.iqsp-011.

[43] Photography Electronic Still-Picture Cameras Resolution Measurements, ISO Standard 12233, 2000.

[44] T. Osborne, V. Ramachandra, K. Atanassov, and S. Goma, "Introducing the cut-out star target to evaluate the resolution performance of 3D structured-light systems," *Proc. SPIE*, vol. 8650, pp. 213–219, Mar. 2013, Art. no. 86500P.

[45] D. Williams, "R10 criteria: A simple single valued MTF performance metric for reporting DSC pixel count," in *Proc. ISO TC42 Conf.*, Sweden, Sweden, Jun. 2004.

[46] E. Abbe, "Beiträge zur theorie des mikroskops und der mikroskopischen wahrnehmung," *Archiv für Mikroskopische Anatomie*, vol. 9, no. 1, pp. 413–468, Dec. 1873, doi: 10.1007/bf02956173.

[47] B. Boldrini, W. Kessler, K. Rebner, and R. W. Kessler, "Hyperspectral imaging: A review of best practice, performance and pitfalls for in-line and on-line applications," *J. Near Infr. Spectrosc.*, vol. 20, no. 5, pp. 483–508, Oct. 2012, doi: 10.1255/jnirs.1003.

[48] G. Yang et al., "The DOM generation and precise radiometric calibration of a UAV-mounted miniature snapshot hyperspectral imager," *Remote Sens.*, vol. 9, no. 7, p. 642, Jun. 2017, doi: 10.3390/rs9070642.

[49] P. Geladi, J. Burger, and T. Lestander, "Hyperspectral imaging: Calibration problems and solutions," *Chemometric Intell. Lab. Syst.*, vol. 72, no. 2, pp. 209–217, Jul. 2004, doi: 10.1016/j.chemolab.2004.01.023.

[50] D. Nouri, Y. Lucas, and S. Treuillet, "Calibration and test of a hyperspectral imaging prototype for intra-operative surgical assistance," *Proc. SPIE*, vol. 8676, pp. 229–237, Mar. 2013.

[51] A. Noviyanto and W. H. Abdulla, "Segmentation and calibration of hyperspectral imaging for honey analysis," *Comput. Electron. Agricult.*, vol. 159, pp. 129–139, Apr. 2019, doi: 10.1016/j.compag.2019.02.006.

[52] (2021). *Encapsulated Gray Scale Standards—Avian Technologies*. Accessed: Jun. 3, 2021. [Online]. Available: https://aviantechnologies.com/product/encapsulated-gray-scale-standards/

[53] (2021). *Reflectance Wavelength Calibration Standards—Avian Technologies*. Accessed: Jun. 2, 2021. [Online]. Available: https://aviantechnologies.com/product/reflectance-wavelength-calibration-standards/

[54] P. D. Burns, "Tone-transfer (OECF) characteristics and spatial frequency response measurements for digital cameras and scanners," *Proc. SPIE*, vol. 5668, pp. 123–128, Jan. 2005.

[55] W. F. Hsu, K. W. Chuang, and Y. C. Hsu, "Comparisons of the camera OECF, the ISO speed, and the SFR of digital still-picture cameras," *Prco. SPIE*, vol. 4080, pp. 104–111, 2000.

[56] Photography-Electronic Still Picture Cameras-Methods for Measuring Opto-Electronic Conversion Functions (OECFs), ISO Standard 14524, 2009.

[57] O. Pekkala, T. Pulli, A. Kokka, and E. Ikonen, "Setup for characterising the spectral responsivity of Fabry–Pérot-interferometer-based hyperspectral cameras," *Metrologia*, vol. 56, no. 6, Dec. 2019, Art. no. 065005, doi: 10.1088/1681-7575/ab3fd1.

[58] L. Gao, L. Cao, Y. Zhong, and Z. Jia, "Field-based high-quality emissivity spectra measurement using a Fourier transform thermal infrared hyperspectral imager," *Remote Sens.*, vol. 13, no. 21, p. 4453, Nov. 2021, doi: 10.3390/rs13214453.

[59] R. Leon et al., "VNIR–NIR hyperspectral imaging fusion targeting intraoperative brain cancer detection," *Sci. Rep.*, vol. 11, no. 1, Oct. 2021, Art. no. 19696, doi: 10.1038/s41598-021-99220-0.

[60] S. George et al., "A study of spectral imaging acquisition and processing for cultural heritage," in *Digital Techniques for Documenting and Preserving Cultural Heritage*. Amsterdam, The Netherlands: Arc Humanities Press, 2017, doi: 10.1515/9781942401353-012.

[61] F. van der Meero and W. Bakker, "Cross correlogram spectral matching: Application to surface mineralogical mapping by using AVIRIS data from cuprite, Nevada," *Remote Sens. Environ.*, vol. 61, no. 3, pp. 371–382, Sep. 1997.

[62] F. van der Meer, "The effectiveness of spectral similarity measures for the analysis of hyperspectral imagery," *Int. J. Appl. Earth Observ. Geoinf.*, vol. 8, no. 1, pp. 3–17, Jan. 2006, doi: 10.1016/j.jag.2005.06.001.

[63] G. Lu and B. Fei, "Medical hyperspectral imaging: A review," *J. Biomed. Opt.*, vol. 19, no. 1, Jan. 2014, Art. no. 010901, doi: 10.1117/1.jbo.19.1.010901.

[64] B. Fei, "Hyperspectral imaging in medical applications," in *Data Handling in Science and Technology*, vol. 32. Amsterdam, The Netherlands: Elsevier, 2020, pp. 523–565.

[65] S. J. Choquette, D. L. Duewer, L. M. Hanssen, and E. A. Early, "Standard reference material 2036 near-infrared reflection wavelength standard," *Appl. Spectrosc.*, vol. 59, no. 4, pp. 496–504, Apr. 2005, doi: 10.1366/0003702053641414.

[66] *ADIMEC-1000m Operating and Technical Manual*, Adimec Adv. Image Syst. B.V., Eindhoven, The Netherlands.

[67] S. Ram, E. S. Ward, and R. J. Ober, "Beyond Rayleigh's criterion: A resolution measure with application to single-molecule microscopy," *Proc. Nat. Acad. Sci. USA*, vol. 103, no. 12, pp. 4457–4462, Mar. 2006, doi: 10.1073/pnas.0508047103.

[68] A. Stacey and C. Pask, "Spatial-frequency response of a photoreceptor and its wavelength dependence i coherent sources," *J. Opt. Soc. Amer. A, Opt. Image Sci.*, vol. 11, no. 4, p. 1193, Apr. 1994, doi: 10.1364/josaa.11.001193.

Laura Quintana-Quintana received the bachelor's degree in biomedical engineering from the University Carlos III of Madrid, Madrid, Spain, in June 2019, and the master's degree in applied electronics and telecommunications research from the University of Las Palmas de Gran Canaria, Las Palmas de Gran Canaria, Spain, in 2020, where she is currently pursuing the Ph.D. degree in bioengineering with the Integrated Systems Design Division, Research Institute for Applied Microelectronics.

Gonzalo Rosa Olmeda received the bachelor's degree in electronics of communications engineering and the master's degree in Internet of Things (IoT) from the Universidad Politécnica de Madrid (UPM), Madrid, Spain, in 2020 and 2021, respectively, where he is currently pursuing the Ph.D. degree with the Electronic and Microelectronic Design Group (GDEM), Software Technologies and Multimedia Systems for Sustainability (CITSEM) Research Center.

His research interests are related to microscopic hyperspectral imaging applied to histopathology applications and digitalization 4.0 of aquaculture facilities.

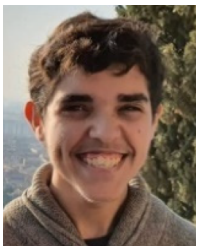

Javier Santana-Nunez received the bachelor's degree in industrial electronics and automation engineering from the University of Las Palmas de Gran Canaria (ULPGC), Las Palmas de Gran Canaria, Spain, in 2023, where he is currently pursuing the M.Sc. degree in intelligent systems and numerical applications applied to engineering. He developed his bachelor thesis at the Research Institute for Applied Microelectronics (IUMA), ULPGC, focusing on designing and evaluating hyperspectral image registration techniques.

He is currently working at IUMA as a Researcher and starting his Ph.D. thesis. His research interests are related to microscopic hyperspectral imaging applied to biological sample analysis, especially for histopathology applications.

Miguel Chavarrías received the Ph.D. degree from the Universidad Politécnica de Madrid (UPM), Madrid, Spain, in 2017.

He is currently an Associate Professor at UPM, where he has been with the Electronics and Microelectronics Design Group (GDEM) since 2011 and the Software Technologies and Multimedia Systems for Sustainability (CITSEM) Research Center since 2012. He has authored more than 30 journal articles and conference papers. He has participated in more than 15 research projects in competitive calls and more than ten contracts with the industry. His research interests include edge computing, hyperspectral imaging, computer vision, and machine learning.

Samuel Ortega received the bachelor's degree in telecommunication engineering and the M.Sc. and Ph.D. degrees in telecommunication technologies from the University of Las Palmas de Gran Canaria, Las Palmas de Gran Canaria, Spain, in 2015, 2016, and 2021, respectively.

In 2021, he started to work as a Researcher at the Norwegian Institute of Food, Fisheries and Aquaculture Research, Tromsø, Norway. His research interests are the use of hyperspectral imaging for medical and food quality applications.

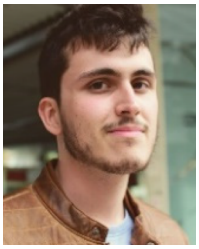

Jaime Sancho received the M.Sc. and Ph.D. degrees (cum laude) in systems and services engineering for the information society from the Universidad Politécnica de Madrid (UPM), Madrid, Spain, in 2018 and 2023, respectively.

He is currently a Teacher and a Research Assistant (Ayudante) at the Telematics and Electronics Engineering Department (UPM). He develops his research career at the Research Center in Software Technologies and Multimedia Systems for Sustainability (CITSEM), UPM. His main research interests include biomedical real-time systems, computer vision applied to immersive video, and GPU computing.

Dr. Sancho is a member of CITSEM.

Himar Fabelo received the master's degree in telecommunication engineering and the Ph.D. degree in telecommunication technologies from the University of Las Palmas de Gran Canaria (ULPGC), Las Palmas de Gran Canaria, Spain, in 2014 and 2019, respectively.

He has conducted his research activity at the Institute for Applied Microelectronics, ULPGC. Currently, he works in the STRATUM EU project as an Assistant Coordinator and a PI at the Fundación Canaria Instituto de Investigación Sanitaria de Canarias (FIISC), Las Palmas de Gran Canaria. He has published more than 50 journal articles and 60 international conference papers in the field of medical technology, particularly in the application of artificial intelligence and hyperspectral imaging for cancer diagnosis in various medical applications.

Dr. Fabelo received the Juan de La Cierva Formación Post-Doctoral Grant at FIISC in 2022.

Eduardo Juárez (Member, IEEE) received the Ph.D. degree from the École Polythecnique Fédéral de Lausanne (EPFL), Lausanne, Switzerland, in 2003.

From 1994 to 1997, he worked as a Researcher at the Digital Architecture Group, Universidad Politécnica de Madrid (UPM), Madrid, Spain, and was a Visiting Researcher at ENST, Brest, France, and the University of Pennsylvania, Philadelphia, PA, USA. From 1998 to 2000, he worked as an Assistant at the Integrated Systems Laboratory (LSI), EPFL. From 2000 to 2003, he worked as a Senior Systems Engineer at the Design Centre, Transwitch Corporation, Geneva, Switzerland, while continuing his research toward the Ph.D. degree at EPFL. In December 2004, he joined UPM as a Post-Doctoral Researcher, where he has been an Associate Professor since 2007. He has co-authored one book and authored or co-authored more than 100 articles and contributions to technical conferences. He has participated in more than 15 competitive research projects and 20 noncompetitive industrial projects. His research activity is mainly focused on hyperspectral imaging for health applications, real-time depth estimation and refinement, and heterogeneous high-performance computing.

Gustavo M. Callico (Senior Member, IEEE) received the M.S. degree in telecommunications engineering and the Ph.D. and European Doctorate degrees from the University of Las Palmas de Gran Canaria (ULPGC), Las Palmas de Gran Canaria, Spain, in 1995 and 2003, respectively.

Since 2022, he has been a Full Professor at ULPGC and has developed his research activities at the Institute of Applied Microelectronics (IUMA). He has co-authored seven book chapters and authored or co-authored more than 200 articles (83 JCR articles) and contributions to technical conferences (134 conferences). He has participated in 27 competitive research projects (six as PI) and holds two international patents. His current research areas include hyperspectral systems for cancer detection, artificial intelligence algorithms, real-time super-resolution algorithms, synthesis-based design for SOCs and circuits for multimedia processing, and video coding standards.